DOI: https://doi.org/10.2138/am-2019-6699

Revision 1

Origin of milky optical features in type IaB diamonds: dislocations, nano-inclusions, and polycrystalline diamond

Tingting Gu[1,*], Hiroaki Ohfuji[2], and Wuyi Wang[1]

[1]Gemological Institute of America (GIA), 50 W. 47th Street, New York, NY, 10036, USA

[2]Geodynamics Research Center (GRC), Ehime University, Matsuyama, 790-8577, Japan

* tgu@gia.edu

ABSTRACT

The milky appearance shown by certain type IaB diamonds has been subjected to several recent studies but the origin of this feature is not fully understood. Here several type IaB diamonds with milky appearance have been studied by cathodoluminescence (CL), electron backscatter diffraction (EBSD), and transmission electron microscopy (TEM). CL of several hazy type IaB diamonds shows scattered or orientated micro-sized spots or short linear luminescence features. TEM observation revealed that those spots and linear features are caused by dislocation loops that are likely responsible for the hazy appearance of the host diamonds. It also shown that type IaB diamonds with a cloudy appearance contain nano-sized inclusions with negative crystals of octahedral shape. Some of these negative crystals contain a precipitate that can be explained by a compressed disordered cubic δ-N_2 phase observed by high-resolution TEM. In one of the milky IaB diamonds with platelet defects, polycrystalline areas composed of columnar diamond crystals elongated radially in [110], similar to ballas diamond, were revealed by EBSD. Taking into account these observations, it is suggested that the dislocation loops, nano-sized inclusions (negative crystals) and/or characteristic grain boundaries of the radiating fibrous crystals would be

the origins for the milky appearance of the type IaB diamonds studied here. Those results add complementary explanation accounting for the milkiness of type IaB diamonds studied before.

Key words: Type IaB diamonds, milky, dislocations, voidites, polycrystalline diamond

INTRODUCTION

The origin of milky diamonds is enigmatic. Unlike diamonds with intense fluorescence that creates an "oily" appearance, milky diamonds contain areas with distinct textures, scattering light and resulting in a hazy or cloudy appearance. With dense "clouds" inside, they can be termed "fancy white" diamonds. The exact cause of their opacity is not fully understood. In previous studies, the term "cloudy" has been used to refer to fibrous diamonds or describe diamonds with submicroscopic internal inclusions. Extensive studies have shown that those frosted zones are filled with disk- crack-like graphite inclusions (Rakovan et al. 2014) or high-density fluids (HDFs) from a deep origin, with compositions ranging between carbonatitic and saline end-members (Navon et al., 1988; Izraeli et al. 2001; Klein-BenDavid et al. 2007; Tomlinson et al. 2009; Logvinova et al. 2011). However, cloudy inclusions filled with HDFs usually appear gray or black, while the milky diamonds are generally white in color, suggesting a different filling.

It has been noticed that milky white diamonds are most often type IaB (Fritsch 1998), with nitrogen in B-aggregates (four nitrogen atoms around a single vacancy, Loubser and van Wyk, 1981). The development of B centers is usually accompanied by the formation of platelets, planar defects in {001} planes that measure a few nanometers to a few micrometers in diameter (Clackson et al.,1990; Speich et al., 2017). In some pure type IaB diamonds, that have been termed "irregular" (Woods 1986), platelets have experienced degradation and may be absent completely. Platelet degradation is often accompanied by the formation of voidites (e.g. Barry et al. 1987). Previous studies have confirmed that voidites and nano-inclusions can be found in type IaB diamonds with milky zones (Rudloff-Grund et al. 2016; Navon et al. 2017). However, the composition of those nano-inclusions is still a subject of debate. Electron energy loss spectroscopy (EELS; Bruley and Brown 1989) and energy- dispersive X-ray spectroscopy studies (EDX; Rudloff-Grund et al. 2016) reveal the presence of nitrogen in the voidites. Based on moiré patterns, the material filling the voidites has been identified as NH_3 (Barry 1986; Hirsch et al. 1986a) or a tetragonal N_2 phase (Luyten et al. 1994; Navon et al. 2017). If such voidites are the products of platelet degradation, elements that constitute the platelets should be present in the voidites or alongside the dislocation loops. However, the structure and composition of the platelets are still unclear. In previous studies, the structural model of platelets with a nitrogen double layer (Lang 1964) was excluded because EELS investigations have shown that the concentration of nitrogen within the platelets is too low to fit with this model (Berger and Pennycook 1982). The generally accepted platelet model is that of a pentagonal interstitial carbon arrangement in the {100} planes as proposed by Humble (1982). Theoretical studies have indicated that the strain associated with small platelets could lead to shallow electronic gap levels that could promote optical transitions from point defects such as nitrogen and vacant sites close to the platelet (Goss et al. 2003). Investigation of the products from platelet degradation would provide more information about their constitution.

In milky diamonds, some contain clusters and areas of cloudy inclusions that are generally visible as very small whitish pinpoints under microscopic observation (Fig. 1). However, in some milky diamonds, no inclusions are visible even with high magnification up to 200×, and the diamonds generally display a slightly hazy appearance (Fig. 1). The different optical features might indicate diverse causes for their milky appearance. Although platelet degradation is often

This is a preprint, the final version is subject to change, of the American Mineralogist (MSA)
Cite as Authors (Year) Title. American Mineralogist, in press.
DOI: https://doi.org/10.2138/am-2019-6699

associated with milky type IaB diamonds, a subgroup of milky diamonds shows sharp platelet peaks, and therefore the cause of their milky appearance is still unclear. To gain a comprehensive understanding of the various origins of the milky features in type IaB diamonds, we examined their optical and structural properties through cathodoluminescence (CL) imaging and transmission electron microscopy (TEM), and investigated their micro-textures by electron backscatter diffraction (EBSD). Based on the results, we discuss origins of the milky appearance in type IaB diamonds and the implications in diamond-forming processes.

METHODS

Sample characteristics

Samples were collected from diamonds submitted by clients to GIA's laboratory for screening; rough diamonds and faceted diamonds were cut into plates for detailed study. We were able to have a close look of samples listed in Table 1 and six of them were cut into plates. All plates except the one with mineral inclusions on the surface were cleaned in a mixture of HCl and $NaNO_3$ for one hour at 100°C. The carat weight, clarity grade, and internal characteristics of each stone are listed in Table 1. Features of FTIR and photoluminescence spectra of those diamonds have been detailed in our previous study (Gu and Wang 2018), and FTIR spectra of all samples are provided in supplementary material (Fig. S1). All samples were typical milky type IaB diamonds that contained hazy or cloudy areas. Under high magnification, no inclusions could be resolved with the microscope in the hazy areas; in contrast, whitish spots were spread throughout the cloudy area.

CL images

Experiments were performed at GIA using a Zeiss EVO MA10 scanning electron microscope (SEM) equipped with a high-resolution CL system. The acquisition of digital grayscale panchromatic CL images was achieved using a multichannel analyzer at room temperature, operating in variable pressure mode with the chamber pressure typically at 20 Pa. Images were collected with a variable pressure secondary electron (VPSE) detector at zero bias, using 15–20 kV accelerating voltage and specimen probe currents between 1 and 20 nA. A typical probe current of 100 pA and a voltage of 15 kV were used for most samples, while a smaller voltage of 10 kV was used to increase the resolution for fine textures.

TEM analysis

TEM foils were prepared by a focused ion beam (FIB) system (JOEL JEM- 9310FIB). The detailed procedure of FIB milling for TEM foil preparation is described elsewhere (e.g., Ohfuji et al. 2010). Each foil has a dimension of approximately 10 × 7 × 0.1 μm. Transmission electron microscopy was carried out using a JEOL JEM-2010 instrument at Ehime University and using a JEOL 2100F instrument at the Center for Functional Nanomaterials (CFN) at the Brookhaven National Laboratory; both equippedwith a field emission gun (FEG), operated at an accelerating voltage of 200 kV. Generally, bright- and dark-field images as well as high-resolution images were acquired as energy-filtered images applying a 20 eV window to the zero loss peak. Diffraction data were calculated from high-resolution images using the fast Fourier transform algorithm (FFT).

EBSD analysis

FE-SEM measurements were carried out on a JEOL JSM-7000F instrument equipped with a Nordlys EBSD detector at Ehime University. Channel 5.0 software was used for data acquisition and analysis. For EBSD using the SEM, an accelerating voltage of 15 kV, a beam current of 4.0 nA, and a working distance of 15 mm were applied for the analysis. The sample was coated with carbon of ~10 nm thickness. Prior to the analysis, an orientation contrast (fore-scattered electron) image was taken by photodiode detectors located at the upper edge of the EBSD camera. Orientation maps were obtained with a step size of 2 or 3 μm by indexing a maximum of eight diffraction lines detected from each Kikuchi pattern. After each analysis, "Tango" and "Mambo" components from the Channel 5.0 software were used to draw an orientation map and pole figure(s) respectively.

RESULTS

CL features

The descriptions of grayscale CL images collected at room temperature for each sample are summarized in Table 1. All samples with a hazy area or "clouds that are not shown" displayed pinpoints under grayscale CL. Some luminescent pinpoints can be resolved as short lines under high magnification. Those luminescent short lines were either straight or curved, usually ranging in size from a few microns to ten microns in size, and could form sets of lines parallel with each other (Fig. 2b-c). Some were oriented in certain crystallographic directions (Fig. 2a–c). Those short lines were often observed in the black areas of the grayscale CL images (Fig. 2b), and some were distributed between the boundaries of black and white regions (Fig. 2d). Some of the pinpoints could also be observed in growth zone areas. They were confined to a small area or spread throughout the whole diamond. Platelet peaks were not observed in FTIR spectra in those diamonds with luminescent pinpoints throughout the whole stones (i.e., 890000048675, 110208618119), while one sample (890000102598) with pinpoints in a small area showed a very small residual peak at 1367.7 cm^{-1} (Table 1, Fig. S1). No typical CL features were observed for diamonds with cloudy inclusions that could be recognized as whitish points under the microscope.

TEM results

FIB foils were prepared from the hazy areas that showed distinct luminescent pinpoints under grayscale CL and from the cloudy areas where tiny whitish pinpoints could be observed under the microscope. TEM images from the hazy areas showed only dislocation loops (Fig. 3a–b). No inclusions or voidites were observed in these FIB foils. Strain contrast was observed at the edge of the dislocations, which showed a typical "coffee-bean" contrast (Hirsch et al. 1965). On the other hand, nano-inclusions of ~20 to 200 nm diameter were observed in the FIB foils cut from the cloudy areas (Fig. 3c). They show octahedral (Fig. 3d), elongated (Fig. 3e–f), or rounded (Fig. 3c) shapes. Most of the octahedral nano-inclusions were 20 to 30 nm in diameter, whereas some were as large as 100 nm (Fig. 3d). They were usually aligned parallel to {111} faces (Fig. 3d). We also observed an inclusion with a rounded outline and a rhombic projection inside (Fig. 3c). Inclusions with elongated shape were as small as 20–30 nm in dimension (Fig. 3d, f), while some of them were up to 200 nm (Fig. 3e).

Fig. 4 shows two high-resolution TEM (HRTEM) images taken from exactly the same region as one of the nano-inclusion, with slightly different focus conditions, where faint lattice fringes were recognized in two directions inside the nano-inclusions. The *d*-spacings of the fringes (2.39 and 2.63 Å) obtained from the images by FFT conversion cannot be indexed by the diamond lattice, and therefore they are derived from an additional crystalline phase precipitated inside the negative crystal.

EBSD results

Kikuchi patterns indicated that all samples were single-crystal diamond except for one sample that showed a sharp residual platelet peak in its FTIR spectrum (sample 110207975364). EBSD mapping revealed that this sample had a granular texture with distinct grain boundaries and grain sizes ranging from ~10 to 200 μm (Fig. 5). Approximately 611 grains were detected in the analyzed region and the average grain size is 50 μm according to the EBSD statistical results. Fig. 6 shows pole figures projected along the <100>, <110>, and <111> planes of diamond, where a strong preferred orientation of [110] was observed almost normal to the orientation map. This suggests that the observed granular domains may be cross-sections of fibrous or columnar crystals that are elongated in the [110] direction perpendicular to the sample (section) surface.

DISCUSSIONS

Previous experiments by other authors have shown that dislocation loops may form at high temperatures close to the graphite-stable region during the platelet degradation process. The conversion of platelets into dislocations may take place by the dislocation reaction (Hirsch et al. 1986b)

$$a_0[00f] + \tfrac{1}{2} a_0[01(1-2f)] \rightarrow \tfrac{1}{2} a_0[011] \quad (1)$$

where f is the matrix displacement at the platelet. Under perfect conditions, a dislocation loop of Burgers vector $\tfrac{1}{2} a_0[011]$ will form and the additional (004) layer will be introduced in the process. Based on the results from previous calculations (Hirsch et al. 1986b) it was proposed that the increase of the dislocation with Burgers vector would be accompanied by the release of vacancies that are subsequently trapped at A centers, resulting in relatively mobile VN_2 defects (H_3 center, Mainwood 1994). In our study, platelet peaks are absent from samples with luminescent pinpoints throughout the diamond under grayscale CL, implying that the platelet peak has been degraded completely. TEM images revealed that these luminescent pinpoints are associated with dislocation loops ranging in tens to hundreds of nanometers. The natural dislocation loops are comparable in shape and size with man-made dislocation loops produced from platelet degradation (Evans et al. 1995). Although the reason for their luminescence under CL is still unclear, the vacancy-related defects likely play a role. In our previous study, a zero phonon line (ZPL) at 490.7 nm was observed on those discrete features, a sign that the ZPL at 490.7 nm is associated with dislocation loops. ESR results show that the ZPL at 490.7 nm correlates with the signal from dangling bonds in the dislocation cores (Nadolinny et al. 2009). Photoluminescence mapping results indicate that the peak area ratio of the line at 490.7 nm positively correlates with that at 496 nm (H_4 center, N_4V_2 defect, Mainwood 1994), but no correlation with H_3 defects is seen (Gu and Wang 2018). The presence of the ZPL at 490.7 nm associated with the luminescent pinpoints would imply that the dislocation loops developed from platelet degradation are associated with dangling bonds and vacancy- related defects. The luminescent pinpoints are relatively dense in the CL image, indicating that dislocation loops are well developed throughout the diamond. They may potentially scatter light and cause a hazy appearance in their host diamonds. However, those dislocation loops might not be recognized under the microscope due to their lack of three-dimensional geometry.

The presence of nano-inclusions was also found to be responsible for the milky nature of type IaB diamonds studied. Their octahedral or elongated morphology and relatively large size (up to 200 nm) make them easier to be seen as cloudy areas of pinpoints under the microscope. Previous studies reported that man-made negative inclusions can be created by platelet degradation (Evans et al. 1995). Those inclusions, called voidites are mostly less than 10 nm in size and are usually found on the dislocation loops (Evans et al. 1995). Voidites have been considered by-products of platelet degradation. According to equation (1), the formation of an additional (004) layer during the development of dislocation loops will create the same number of vacancies as there are atoms in the plane. Since the atomic density of the voidites is about a half of the diamond lattice, the number of vacancies produced during the conversion of platelets by artificial heat treatment is roughly equal to the number required to form the voidites observed by Evans et al. (1995). However, the nano-inclusions observed in natural samples (Kaminsky et al. 2013, 2015) are much larger than those produced experimentally by platelet degradation. In recent studies of Brazilian diamonds from the Juina area (Rudloff-Grund et al. 2016), a distinctly bimodal size distribution of the nano-inclusions was observed. Whereas the suite of octahedral nano-inclusions is generally around 20–30 nm, the larger nano-inclusions were up to 150–200 nm and mostly elongated. In our studies, the elongate inclusions were found to be mostly small (around 20–30 nm) like the case of the octahedral inclusions, but occasionally large (up to 200 nm). Those nano-inclusions can present independently and are usually located at a distance from dislocation loops, implying their syngeneic origin (Kaminsky et al. 2013, 2015), i.e. the fluid was directly trapped during the formation of the host.

The materials that precipitated within nano-inclusions (negative crystals) in type IaB diamonds have been identified mainly by HRTEM and Raman spectroscopy in previous studies (Barry 1986; Luyten et al. 1994, Rudloff-Grund et al. 2016; Navon et al. 2017). The *d*-spacings obtained from the lattice fringes on the HRTEM images of precipitates suggest a few candidates for the crystalline phases. One of them is a solid NH_3 phase having a *d*-spacing of about 2.4 Å, which compares well with that of a cubic NH_3 phase compressed to 3.16 GPa (d_{200} = 2.38 Å) (Barry 1986). Although a much larger fringe of 1.41 nm was observed in nano-inclusions in Juina diamond, it might be caused by the lattice of the stressed diamond itself (Rudloff-Grund et al. 2016). In another recent study on Juina diamond (Navon et al. 2017), the *d*-spacings (2.4 and 2.5 Å) obtained from the lattice fringes were interpreted to be derived from a tetragonal γ-N_2 phase (Schuch and Mills 1970) with unit cell dimensions of a = 3.66 Å and c = 4.98 Å, whereas the observed intersection angles did not match with the cubic symmetry. Raman spectroscopy showed a sharp peak at ~2355 cm^{-1} and a weaker peak at ~2367 cm^{-1}, which can be assigned to υ_2 and υ_1 vibrational modes of the tetragonal δ-N_2 phase, respectively. The residual pressure estimated from the Raman shift obtained from the inclusion was about 10.9 GPa (Navon et al. 2017). In our study, the *d*-spacings obtained from HRTEM images are 2.39 Å and 2.63 Å, which deviate slightly from the results of Navon et al. (2017) but are similar to the results of Luyten et al. (1994) who reported *d*-spacings of 2.40 and 2.64 Å. Luyten et al., (1994) proposed a tetragonal crystal structure for the non-equilibrium modification of the solid N_2 phase found in their study. However, we found that the *d*-spacings obtained in our study are very close to the disordered cubic δ-N_2 phase ($d_{(1\text{-}20)}$ = 2.63 Å and $d_{(21\text{-}1)}$ = 2.40 Å) observed at 9.5 GPa and room temperature by X-ray diffraction in a diamond anvil cell (Hanfland et al. 1998). Therefore, it is likely that the material filling the octahedral nano-inclusions is a cubic δ-N_2 phase under compression to an equivalent high pressure. This residual pressure (~ 9.5 GPa) held in the inclusion is comparable to that (10.9 GPa) reported in the previous study (Navon et al. 2017), suggesting that the inclusions might have been trapped under similar *P*-*T* conditions.

In addition to the irregular diamonds, milkiness is also observed in type IaB diamonds with sharp platelet peaks, that have not undergone complete platelet degradations. Those diamonds show a poly-crystalline texture composed of elongated crystals of 50–200 μm, in which the light passing through is scattered at the grain boundaries resulting in the milky appearance. This microstructure is comparable to that shown by a spherulitic polycrystalline diamond called "ballas", which consists of columnar to fibrous crystals radiating from a core (DeVries and Robertson 1985; Lux et al. 1997). The elongation direction of the crystals in ballas was observed by X-ray diffraction to be [110] (Trueb and Barrett 1972), which is indeed identical to the case of the milky type IaB diamonds under investigation. The formation of ballas has been explained by the "hailstone model", which requires a high under-cooling condition and/or a low diffusion rate. According to this model, the extremely fast quenching rate due to impurity enrichment will lead to a passive boundary layer that will reduce the diffusion rate to stimulate a radial (spherulitic) growth of the crystals (Lux et al. 1997). Besides, the occurrence of such spherulitic polycrystalline diamonds is likely restricted to the oldest parts of the continental crust (cratons, generally >2.0 Ga) (Haggerty 2014), and the long resident time would allow nitrogen to be fully aggregated. Based on the hailstone (rapid growth) model, their formation might take place as a result of the interaction of hot fluids with cooled materials which enables rapid diamond growth due to significantly undercooling environments. If they stay in a relatively stable mantle condition for a long geological time after the initial formation, it could lead to the aggregation of nitrogen forming the B center.

IMPLICATIONS

Our comprehensive observations by CL, TEM and EBSD suggest that the dominant dislocation loops, nano-inclusions and/or the characteristic grain boundaries formed by radiating fibrous crystals are essential origins for milky features shown by the type IaB diamonds studied here. Detailed studies of the relationship of their inner structures with optical scatterings would provide more insights into the mechanism of their coloration and even find more factors that could contribute to their milkiness. Although our study is limited to type IaB diamonds, we expect that other diamonds with similar textures would also have a milky appearance. The milky type IaB diamonds studies here are one of the major sources of our knowledge on volatiles in diamond and have significant geological implications. The precipitate found in octahedral nano-inclusions (negative crystals) in this study can be explained by a disordered cubic δ-N_2 phase under compression to ~10 GPa. Similar high residual pressures were also reported in nitrogen inclusions in “super-deep” diamonds from Juina, Brazil (Navon et al, 2017). The authors estimated the *P*-*T* conditions of equilibrium between the inclusions and the host diamond using equations of state at mantle geotherm temperatures and concluded that the inclusions are derived from the deepest part of the mantle transition zone at pressures of ~22 GPa. Our results suggest that the present type IaB milky diamonds containing abundant nano-inclusions may also have a very deep origin. Besides, our photoluminescence (PL) results (Gu et al., 2018) revealed that the dominant defects in many milky type IaB diamonds are mainly associated with plastic deformation, which is not inconsistent with a deep origin. In addition, milky features are also found in poly-crystalline type IaB diamonds composed of radiating fibrous crystals similar to ballas. Since the formation of such polycrystalline diamonds likely requires a large driving force such as under undercooling or supersaturated conditions, the milky polycrystalline diamonds may have formed in deep geological settings where the close interaction between C-H-O fluid and crustal/mantle rocks or between two different fluids occurred.

ACKNOWLEDGMENTS

We would like to thank Naomi Uchiyama and Kim Kisslinger for assistance with FIB; Lihua Zhang for technical support with TEM; Tetsuo Irifune for the support of the PRIUS project; Stuart Overlin for editing; Jae Liao for photographing; Adrian Chan for sample polishing; and Ulrika D’Haenens-Johansson, Karen Smit, Evan M. Smith, Christopher M. Breeding, Sally Eaton-Magaña, Paul Johnson, and Kyaw Moe for valuable discussions and suggestions. This research used resources of the Center for Functional Nanomaterials, which is a U.S. DOE Office of Science Facility, at Brookhaven National Laboratory under Contract No. DE-SC0012704.

REFERENCES CITED

Barry, J.C. (1986) Voidites in diamond—do they contain nitrogen? Ultramicroscopy, 20, 169–176.

Barry, J. C., Bursill, L. A., Hutchison, J. L., Lang, A. R., Rackham, G. M., & Sumida, N. (1987). On Voidites: A high-resolution transmission electron microscopic study of faceted void-like defects in natural diamonds. Philosophical Transactions for the Royal Society of London. Series A, 321(1), 361–401.

Berger, S.D., and Pennycook, S.J. (1982) Detection of nitrogen at {100} platelets in diamond. Nature, 298, 635–637.

Bruley, J., and Brown, L.M. (1989) Quantitative electron energy-loss spectroscopy microanalysis of platelet and voidite defects in natural diamond. Philosophical Magazine A, 59, 247–261.

Clackson, S.G., Moore, M., Walmsley, J.C., Woods, G.S., (1990) The relationship between platelet size and the frequency of the B′ infrared-absorption peak in type-Ia diamond. Philosophical Magazine B-Physics of Condensed Matter Statistical Mechanics Electronic Optical and Magnetic Properties 62 (2), 115–128.

DeVries, R.C., and Robertson, C. (1985) The microstructure of ballas (polycrystalline diamond) by electrostatic charging in the SEM. Journal of Materials Science Letters, 4, 805–807.

Evans, T., Kiflawi, I., and Luyten, W. (1995) Conversion of platelets into dislocation loops and voidite formation in Type IaB diamonds. Proceedings: Mathematical and Physical Sciences, 449, 295–313.

Fritsch, E. (1998) The nature of color in diamonds, 25 p. (G.E. Harlow, Ed.) pp. 23–47. The Nature of Diamonds, New York, NY: Cambridge University Press.

Goss, J.P., Coomer, B.J., Jones, R., Fall, C.J., Briddon, P.R., and Öberg, S. (2003) Extended defects in diamond: The interstitial platelet. Physical Review B, 67, 993.

Gu, T., and Wang, W. (2018) Optical defects in milky type IaB diamonds. Diamond and Related Materials, under review.

Haggerty, S.E. (2014) Carbonado: Physical and chemical properties, a critical evaluation of proposed origins, and a revised genetic model. Earth Science Reviews, 130, 49–72.

Hanfland, M., Lorenzen, M., Wassilew-Reul, C., and Zontone, F. (1998) structures of molecular nitrogen at high pressures. Review of High Pressure Scientific Technology, 7, 787–789.

Hirsch, P., Howie, A., Nicholson, R., Pashley, D.W., and Whelan, M.J. (1965) Electron Microscopy of Thin Crystals, 1 p. London, Butterworth.

Hirsch, P.B., Hutchison, J.L., and Titchmarsh, J. (1986a) Voidites in diamond: Evidence for a crystalline phase containing nitrogen. Philosophical Magazine A, 54, L49–L54.

Hirsch, P.B., Pirouz, P., and Barry, J.C. (1986b) Platelets, dislocation loops and voidites in diamond. Proceedings of the Royal Society A: Mathematical, Physical and Engineering Sciences, 407, 239–258.

Humble, P. (1982) The structure and mechanism of formation of platelets in natural type Ia diamond. Proceedings of the Royal Society A: Mathematical, Physical and Engineering Sciences, 381, 65–81.

Izraeli, E.S., Harris, J.W., and Navon, O. (2001) Brine inclusions in diamonds: a new upper mantle fluid. Earth and Planetary Science Letters, 187, 323–332.

Kaminsky, F.V., Wirth, R., and Schreiber, A. (2013) Carbonatitic inclusions in Deep Mantle diamond from Juina, Brazil: New minerals in the carbonate-halide association. Canadian Mineralogist, 51(5), 669–688.

Kaminsky, F.V., Wirth, R., and Schreiber, A. (2015) A microinclusion of lower-mantle rock and some other lower-mantle inclusions in diamond. Canadian Mineralogist, 53(1), 83–104.

Klein-BenDavid, O., Izraeli, E.S., Hauri, E., and Navon, O. (2007) Fluid inclusions in diamonds from the Diavik mine, Canada and the evolution of diamond-forming fluids. Geochimica et Cosmochimica Acta, 71, 723–744.

Lang, A.R. (1964) A proposed structure for nitrogen impurity platelets in diamond. Proceedings of the Physical Society, 84, 871.

Logvinova, A.M., Wirth, R., Tomilenko, A.A., Afanas'ev, V.P., and Sobolev, N.V. (2011) The phase composition of crystal-fluid nanoinclusions in alluvial diamonds in the northeastern Siberian Platform. Russian Geology and Geophysics, 52, 1286–1297.

Loubser, J.H., and Van Wyk, J.A. (1981) Diamond Conference, Reading (unpublished)

Lux, B., Haubner, R., Holzer, H., and DeVries, R.C. (1997) Natural and synthetic polycrystalline diamond, with emphasis on ballas. International Journal of Refractory Metals and Hard Materials, 15, 263–288.

Luyten, W., Van Tendeloo, G., Fallon, P.J., and Woods, G.S. (1994) Electron microscopy and energy-loss spectroscopy of voidites in pure type IaB diamonds. Philosophical Magazine A, 69, 767–778.

Mainwood, A. (1994). Nitrogen and nitrogen-vacancy complexes and their formation in diamond. Physical Review B, 49(12), 7934–7940.

Nadolinny, V.A., Yurjeva, O.P., and Pokhilenko, N.P. (2009) EPR and luminescence data on the nitrogen aggregation in diamonds from Snap Lake dyke system. Lithos, 112, 865–869.

Navon, O., Hutcheon, I. D., Rossman, G. R., and Wasserburg, G. J. (1988). Mantle-derived fluids in diamond micro-inclusions. Nature, 335(6193), 784–789.

Navon, O., Wirth, R., Schmidt, C., Jablon, B.M., Schreiber, A., and Emmanuel, S. (2017) Solid molecular nitrogen (δ-N_2) inclusions in Juina diamonds: Exsolution at the base of the transition zone. Earth and Planetary Science Letters, 1–11.

Ohfuji, H., Okuchi, T., Odake, S., Kagi, H., Sumiya, H., and Irifune, T. (2010) Micro-/nanostructural investigation of laser-cut surfaces of single- and polycrystalline diamonds. Diamond and Related Materials, 19, 1040–1051.

Rakovan, J., Gaillou, E., Post, J.E., Jaszczak, J.A., and Betts, J.H. (2014) Electron microscopy of “giant” platelets on cube planes in diamond. Rocks & Minerals, 89, 993–1012.

Rudloff-Grund, J., Brenker, F.E., Marquardt, K., Howell, D., Schreiber, A., O'Reilly, S.Y., Griffin, W.L., and Kaminsky, F.V. (2016) Nitrogen nanoinclusions in milky diamonds from Juina area, Mato Grosso State, Brazil. Lithos, 265, 57–67.

Schuch, A.F., and Mills, R.L. (1970) Crystal structures of the three modifications of nitrogen 14 and nitrogen 15 at high pressure. The Journal of Chemical Physics, 52, 6000–6008.

Speich, L., Kohn, S.C., Wirth, R., Bulanova, G.P., Smith, C.B. (2017) The relationship between platelet size and the B′ infrared peak of natural diamonds revisited. Lithos, 278-281, 419–426.

Tomlinson, E.L., Müller, W., and EIMF (2009) A snapshot of mantle metasomatism: Trace element analysis of coexisting fluid (LA-ICP-MS) and silicate (SIMS) inclusions in fibrous diamonds. Earth and Planetary Science Letters, 279, 362–372.

Trueb, L.F., and Barrett, C.S. (1972) Microstructural investigation of ballas diamond. American Mineralogist, 57, 1664–1680.

Trueb, L.F., and Butterman, W.C. (1969) Carbonado: a microstructural study. American Mineralogist, 54, 412–425.

Woods, G.S. (1976) Electron microscopy of “giant” platelets on cube planes in diamond. Philosophical Magazine, 34, 993–1012.

Woods, G.S. (1986) Platelets and the infrared absorption of type Ia diamonds. Proceedings of the Royal Society A: Mathematical, Physical and Engineering Sciences, 407, 219–238.

DOI: https://doi.org/10.2138/am-2019-6699

TABLE 1. Summary of milky type IaB diamond samples analyzed in this study

Sample #	Carat weight	Clarity grade	Platelet*	General observations	Clarity description	CL features
110208637198 [a]	2.02	SI_2	-	Hazy	Additional clouds are not shown	Pinpoints
890000048675 [a]	2.93	SI_2	-	Hazy	Clouds are not shown [d]	Oriented pinpoints
880000140049 [a]	1.35	I_1	-	Cloudy/hazy zones	Clouds are not shown	Pinpoints in growth zone
110208742760 [a]	3.34	I_1	-	Cloudy/hazy zones	Additional clouds are not shown	Pinpoints in black area
110208618119 [a]	100.87	-	-	Hazy	Clouds are not shown	Pinpoints
890000102598 [a]	5.55	I_1	1367.7	Hazy	Clouds, pinpoints are not shown	Pinpoints in black area
110208773017 [b]	0.28	SI_2	-	Cloudy/hazy zones	Clouds and hazy area	Pinpoints in black area
110207975362 [b]	0.19	-	-	Hazy	Clouds and hazy area	Pinpoints in black area
110207975359 [b]	0.25	-	-	Cloudy	Clouds	-
110207975361 [b]	0.30	-	1367.7	Cloudy	Clouds	-
110207975363 [b]	0.33	-	1367.7	Cloudy	Clouds	-
110207975364 [b]	0.44	-	1361.2	Cloudy	Clouds	Granular texture
0927 [c]	0.63	-	-	Cloudy/hazy zones	Clouds and hazy area	Pinpoints in hazy area

* Values are given as the FTIR peak position of the platelet defect in wavenumbers (cm^{-1}).

[a] Faceted diamonds; [b] those faceted diamonds were cut into plates; [c] diamond rough.

[d] "Clouds are not shown" means the definite outlines of the clouds cannot be detected under 10× loupe, while the area looks hazy/not fully transparent.

Figure captions

FIGURE 1. Images of all milky type IaB diamonds studied in this paper. Caret weights of each faceted diamonds are given, while images of these samples are not to scale. Microscope images on the right side show typical hazy area in sample 110208618119 under 200× magnification, and cloudy area (indicated by red arrow) in sample 0927 under 100× magnification.

FIGURE 2. Typical grayscale CL images of hazy diamonds, which show luminous pinpoints or short linear defects. (a) CL image of sample 110208618119. (b) CL image of sample 890000102598, size of pinpoints and short lines ranging from a few micros to ~15 micros. (c) CL image of sample 890000048675. Sets of pinpoints form parallel lines. (d) CL image of sample 880000140049. Pinpoints distribute in growth zones. (e) CL image of sample 110208773017. (f) CL image of sample 110207975362. Pinpoints can be observed in growth zones.

FIGURE 3. Typical TEM images of dislocation loops in hazy diamonds (a, b) and nano-inclusions in cloudy diamonds with both octahedral and elongated shapes (c–f). (a) dislocation loop in diamond sample 110208773017. (b) "coffee bean" contrast at the edge of dislocation loop in diamond sample 110207975362. (c) a nano-inclusion with a rounded outline and a rhombic projection inside in sample 110207975359. (d) large octahedral (~100 nm) and small elongated (~30 nm) nano-inclusions in sample 110207975361. (e) large elongated inclusion ~200 nm with octahedral inclusions in sample 110207975363. (f) a group of elongated nano-inclusions with relatively small size below 50 nm.

FIGURE 4. HRTEM image of an octahedral inclusion measuring ~50 nm. Faint fringes can be observed in two directions (6 to 12 o'clock and 3 to 9 o'clock) in (a) and (c). Corresponding FFT images with *d*-spacings calculated from each pattern are given in (b) and (d).

FIGURE 5. EBSD characteristics of polycrystalline diamond: (a) grain boundary map generated by indexing diffraction lines detected from each Kikuchi pattern (b) artificial colors based on different orientations.

FIGURE 6. Pole figures from the mapped area of polycrystalline diamond, based on 114,642 data points, showing that the preferred orientation of the poly-crystals is along the <110> direction.


110208637198
2.02 ct
890000048675
2.93 ct
880000140049
1.35 ct
110208742760
3.34 ct
110208773017
0.28 ct
110208618119
100.87 ct
Hazy area
890000102598
5.55 ct
110207975362
0.19 ct
110207975359
0.25 ct
110207975361
0.30 ct
110207975363
0.33 ct
110207975364
0.44 ct
0927
Cloudy area
500 μm

FIGURE 1.

DOI: https://doi.org/10.2138/am-2019-6699

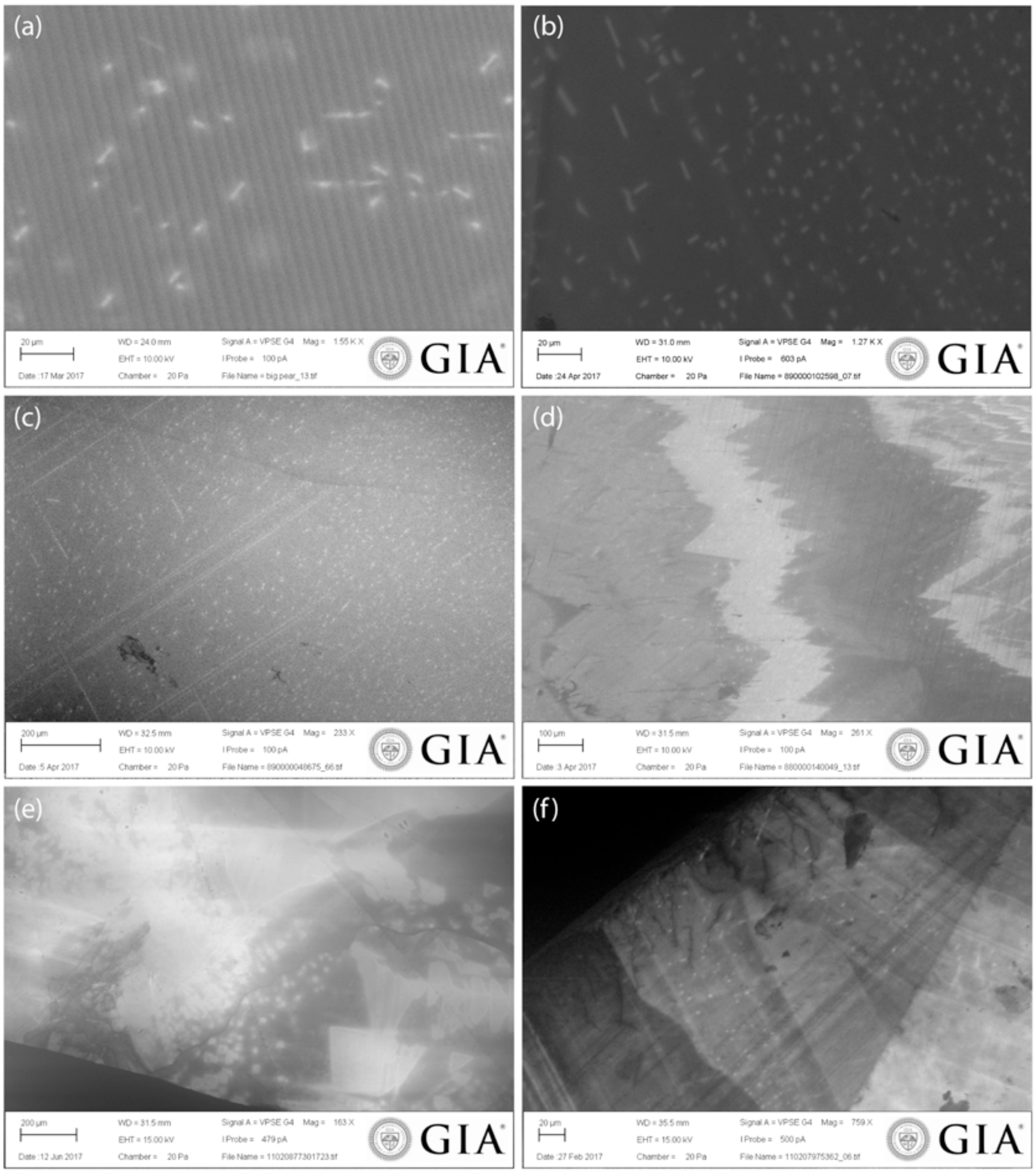

FIGURE 2

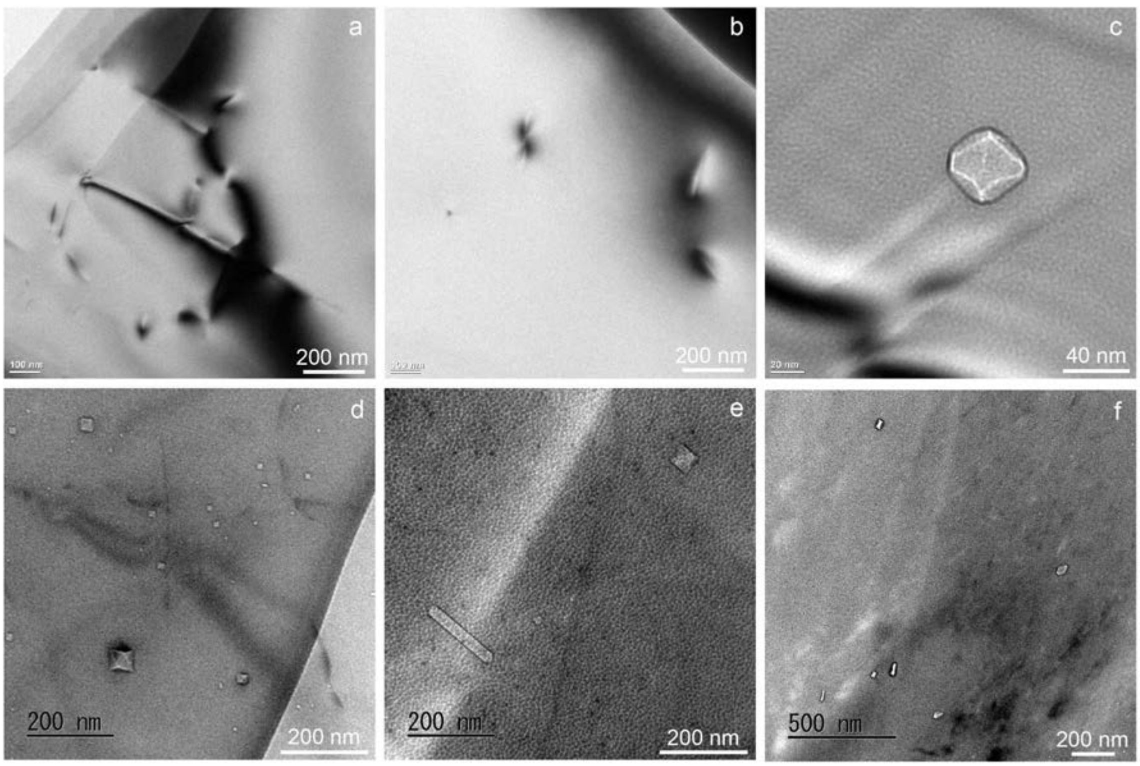
a
200 nm
b
200 nm
c
40 nm
d
200 nm
200 nm
e
200 nm
200 nm
f
500 nm
200 nm

FIGURE 3

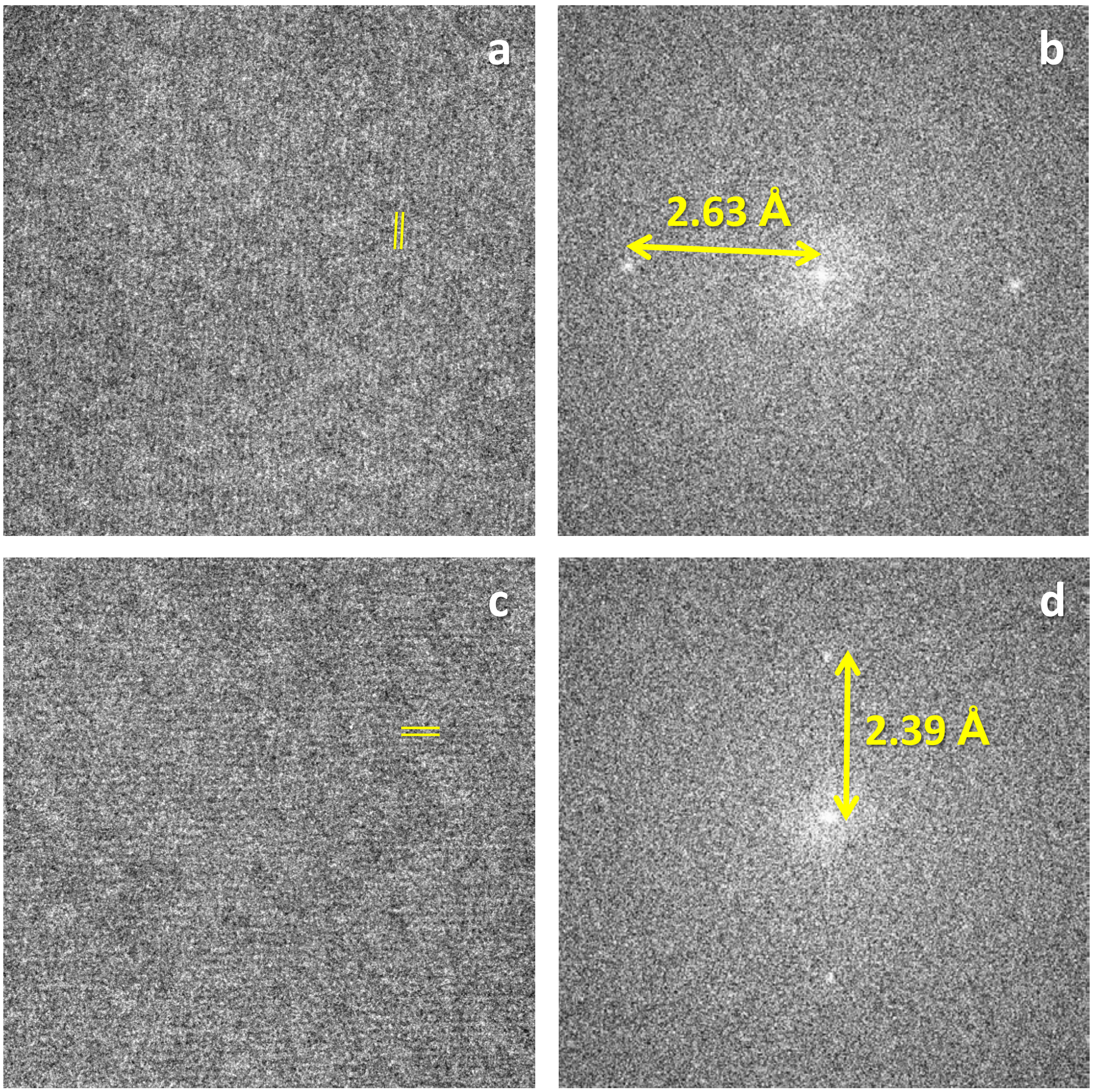

FIGURE 4

DOI: https://doi.org/10.2138/am-2019-6699

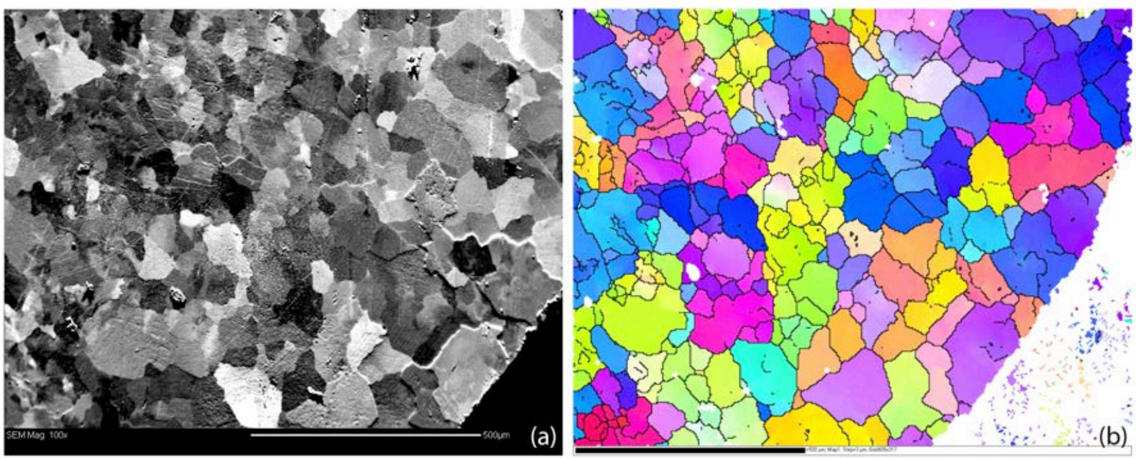

FIGURE 5

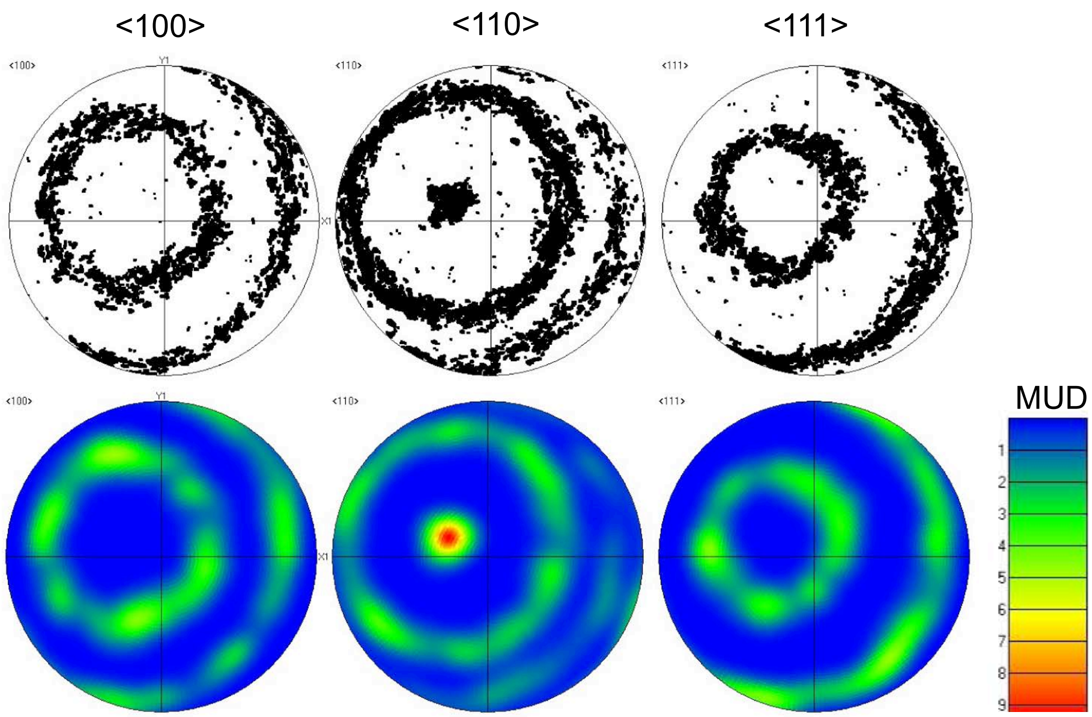

FIGURE 6